Performance and failure analysis of a retrofitted Cessna aircraft with a Fuel Cell Power System fuelled with liquid hydrogen

A.F.B. Abu Kasim[1], M.S.C. Chan[2], E.J. Marek[1*]

[1]Department of Chemical Engineering and Biotechnology, University of Cambridge, Philippa Fawcett Drive, CB3 0AS, UK

[2]Stratospheric Platforms Ltd, Granta Park, Great Abington, CB21 6GP, UK

[*]Corresponding author: ejm94@cam.ac.uk

Abstract

Proton-Exchange Membrane-Fuel Cells (PEM-FC)a are regarded as one of the prime candidates to provide emissions-free electricity for propulsion systems of aircraft. Here, a turbocharged Fuel Cell Power System (FCPS) powered with liquid H_2 (LH_2) is designed and modelled to provide a primary power source in retrofitted Cessna 208 Caravan aircraft. The proposed FCPS comprises multiple PEM-FCs assembled in stacks, two single-stage turbochargers to mitigate the variation of the ambient pressure with altitude, two preheaters, two humidifiers, and two combustors. Interlinked component sub-models are constructed in MATLAB and referenced to commercially available equipment. The FCPS model is used to simulate steady-state responses in a proposed 1.5 h (~350 km) mission flight, determining the overall efficiency of the FCPS at 43% and hydrogen consumption of ~28 kg/h. The multi-stack FCPS is modelled applying parallel fluidic and electrical architectures, analysing two power-sharing methods: equally distributed and daisy-chaining. The designed LH2-FCPS is then proposed as a power system to a retrofitted Cessna 208 Caravan, and with this example analysed for the probability of failure occurrence. The results demonstrate that the proposed “dual redundant” FCPS can reach failure rates comparable to commercial jet engines with a rate below 1.6 failures per million hours.

Keywords: fuel cell propulsion, Liquid H_2, Fuel Cell Power System, failure analysis

1. Introduction

The need for global decarbonisation calls for sustainable and net zero-emissions aviation. For certain classes of aircraft, fuel cells (FC) are a promising technology to provide CO_2-free electrical power [1]; hence, FC-based and hydrogen-fuelled power systems have recently gained prominence as an attractive solution for future carbon-free aircraft. For example, the HyFlyer II project by ZeroAvia, supported by the UK government, focuses on developing a 19-seat FC-powered aircraft following their successful demonstration of a 6-seat hydrogen-electric aircraft, with commercialisation plans in 2023 [2]. Because of their portable nature and moderate operating conditions (60–80℃), Proton-Exchange Membrane-FC (PEM-FC) is considered an attractive, less expensive than batteries [3], option for transportation. For operation in aviation, a practical Fuel Cell Power System (FCPS) requires additional equipment, *i.e.* for reactant delivery and conditioning. As a result, a relatively intricate system design is involved, which should be studied and modelled before the practical implementation of FCPS in aviation.

PEM-FCs typically operate >1 bar absolute, but because ambient pressure (P_{amb}) decreases with altitude (dropping to 0.70 bar at 3.05 km above the sea level); hence, an “air-breathing” FCPSs in aviation should include a compressor to draw and compress the reactant air. During a climbing part of a flight mission, the compressor work increases with the altitude, consuming an increasing amount of power. If the FC stack powers the compressor, then less power is available for other aircraft systems. Alternatively, turbochargers paired with a combustor offer an alternative solution to provide air to FCPS by meeting the compression duty with the work generated by turbines powered by the combustion exhaust. The compressor then no longer depends on the electricity generated by the FC, improving overall system efficiency.

Numerous studies on PEM-FC modelling are available in the literature, differing in the modelling approach. Hoeflinger and Hofmann [4] constructed an empirical model for a 25 kW FCPS testbench to study the air delivery subsystem. Their analysis presented the pressurisation requirement for a PEM-FC, arriving at the parasitic power consumed by the compressor as 10% of the FC-generated power for operations at the ground level. Murugesan *et al.* [5] and Abdin *et al.* [6] investigated the water generation and transport in PEM-FC stacks by constructing a semi-empirical model of a Ballard Mark V 5 kW PEM-FC stack, demonstrating the importance of keeping the PEM-FC humidified to manage FC’s resistive losses. A few modelling studies discussed FC systems in the application context; instead, most published papers focused primarily on the PEM-FC’s operating parameters. For land-based vehicles, Kerviel *et al.* [7] proposed PEM-FC and Solid-Oxide Fuel Cell (SOFC) power systems, with FCs modelled as black-boxes. Models of both FC systems included electric-turbochargers and other auxiliary components, creating interlinked simulation environments. Xun *et al.* [8] modelled a hybrid power system with an FC and a supercapacitor to power an electric vehicle, Honda

Clarity. Although comprehensive for the powertrain system analysis, the published studies focused on ground-level applications, while similar insight into FC-power systems for aircraft is lacking.

Relating to the application of FCPS for aircraft, Guida and Minutillo [9] proposed a design for FCPS-based electrification of aircraft subsystems, satisfying power requirements other than propulsion. The proposed 24 kW FCPS for replacing the auxiliary power unit was designed using commercially available equipment. Kadyk *et al.* analysed the potential of FCPS as a power system for fully electric aircraft, reconfiguring Airbus A320 and Boeing B772 [10]. Both aircraft were analysed looking at representative flight missions, with power requirements >25 MW. However, not much detail on commercial FC stacks or other FCPS components was provided as the power system's modelling was kept to a minimum. Although the need for turbocharging was not mentioned, the listed studies described crucial design considerations for FCPS in aviation, discussing obstacles to overcome and possible approaches for simulating flight missions. Turbocharged FCPS for aircraft applications flying at ~40,000 ft (typical altitude for long-distance passenger aircraft) was assessed by Campanari *et al.* [11] but focusing on the electrification of auxiliary power units rather than propulsion. Atreya *et al.* [12] analysed three different architectures with SOFC, PEM-FC, and internal combustion engine (ICE) for High-Altitude Long-Endurance (HALE) aerial vehicles flying at 60,000 ft above sea level, with all systems powered with liquid H_2 (LH2) as a fuel. The authors discussed and highly recommended turbochargers as an attractive solution to deliver air to the power systems, with compressors being efficiently powered by the shaft work from turbines. However, the turbocharging system was not modelled; hence, a comprehensive assessment of the proposed FCPSs is still missing.

Nevertheless, both Campanari *et al.* [11] and Atreya *et al.* [12] proposed top-level designs for turbocharged PEM-FC systems. The anode side in Campanari *et al.* [11] was proposed to be fed with gaseous H_2 from storage or a reformer of jet fuel, and one-stage turbocharging was implemented on the airside operating above 0.8 bar. After compression, the air passed through a heat exchanger to cool down by exchanging heat with the exhaust from the cathode side. For humidification of the FC, direct water injection was applied only at the cathode. The turbine was powered by combustion off-gases, created by burning a mixture of kerosene and the exhaust H_2 after the cathode. In contrast, Atreya *et al.* [12] included a two-stage turbocharger with intercooling, powering the system with LH_2, and accounting for humidification of both the anode and cathode sides. To power the turbine, a hydrogen combustor was included, taking the fuel directly from storage (LH2), along with unreacted H_2 from the FC stacks.

In a more recent study, an H_2-powered propulsion system with internal combustion reciprocating engine (ICE) [13] was paired with a turbocharger, with detailed turbocharging specifications. Compressor and turbine models for the turbocharger paired with a 90 kW Hydrogen ICE model were used to determine the applicability of the system for a

HALE aircraft. The mechanical power required by the compressors reached ~50 kW, met by the shaft work from the turbines. This is significantly higher than that in ground-level applications, for example, ~2.5 kW of electrical power (kW_{el}) required to compress air for a 25 kW FCPS test bench [4]).

Overall, designing and modelling an entirely FCPS-powered aircraft remains an open and active field of research, especially for turbocharged applications, with research gaps in analysing current equipment capabilities, application of multi-stack FC modules, and the overall reliability of the system. This paper proposes a new architecture for an FCPS powered with LH2, analysing the operation of the presented system with a model constructed in MATLAB. The design is then analysed for the performance during a flight mission and the failure rate. Finally, a potential retrofit option into a commercial passenger aircraft, Cessna 208 Caravan, is proposed.

2. Representative Aircraft and Flight Mission

The Cessna 208 Caravan is a passenger aircraft that can carry up to 14 passengers and uses a single Prattle & Whitney turboprop engine rated at 675 shp (503 kW of mechanical power, kW_{mech}) [14]. Its max altitude is 25,000 ft (7.62 km), but because the cabin is unpressurised, the recommended cruising altitude is 10,000 ft (3.05 km) [15]. The maximum range is ~1900 km and depends on the aircraft's fuel capacity (usable jet fuel weight of 1009 kg). At ≥90% motor efficiency [16], an electric propulsion counterpart will need to be sized at ~560 kW_{el}. This power level can be supported by batteries, as in the recently demonstrated electric variant of the aircraft, eCaravan, which used the 560 kW_{el} magni500 propulsion system with 1 tonne of lithium-ion batteries [17]. The eCaravan version of Cessna 208 has a reduced maximum occupancy of 6 passengers. The reported eCaravan flight demonstration lasted 30 min, requiring at least an equal recharge time. Estimating the energy density of Li-ion batteries to be, optimistically, 265 Wh/kg [18], the demonstrated flight duration appears to be close to the maximum achievable duration for this e-aircraft ($265\ \mathrm{Whkg^{-1}} \times 1000\ \mathrm{kg} \div 560{,}000\ \mathrm{W} \approx 0.5\ h$).

Using the Cessna 208 Caravan's flight manual [19] as a guide, a representative flight mission could be constructed from the typical climb and descent rates, engine rotations per minute and torque, and the related fuel consumption. Here, a short-haul 1.5 h flight is proposed, covering at least 350 km (*e.g.* CDG Paris ↔ Heathrow [20] or equivalent). Figure 1 illustrates the constructed flight mission. This mission is later used to assess the performance of the Cessna 208 Caravan retrofitted with a new FCPS powered with LH2.

Key flight requirements for a 350 km mission:

- Cruising altitude: 10,000 ft (3048 m) with unpressurised cabin,
- $Pow_{takeoff} = 560\ \mathrm{kW}_{el}$ (engine specifications),
- Average climb rate to cruising altitude: 12.25 km/h (translates to ~0.25 h of climbing),

- Average climb gradient to cruising altitude: 55.41 $m_{elevation}$/$km_{distance}$, covering ~55 km of the mission,
- $Pow_{descent} = 323\ \mathrm{kW}_{el}$ (based on the fuel consumption),
- Average descent rate to sea level: 14.63 km/h, lasting ~0.2 h, covering ~45 km of the mission,
- Cruise power: average 390 kW_{el} (max. 488 kW_{el}, min. 332 kW_{el}), calculated as:

$$Pow_{cruise} = \left[Torque(ft.lb) \times RPM \div 5252 \frac{RPM\ ft.lb}{HP}\right] \div 0.9$$

$$P_{cruise} = \left[1400\ ft \cdot lb \times 1750 RPM \div 5252 \frac{RPM\ ft.lb}{HP}\right] \div 0.9$$

$$P_{cruise} \approx 518\ HP \Rightarrow 390\ kW_{el}$$

- Cruising for 1.05 h covering approximately 300 km of the mission.

The maximum distance reaches ~400 km, giving a safe margin for commercial, medium-distance missions.

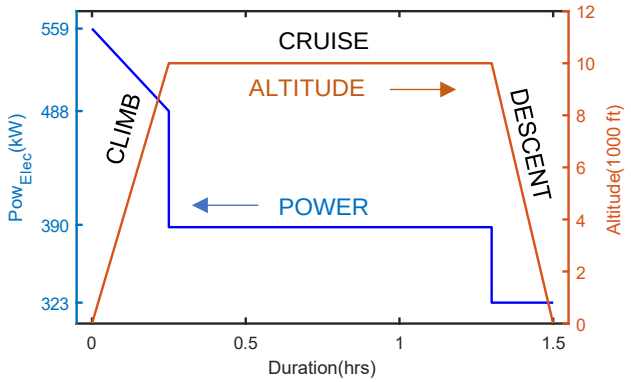

Figure 1. Flight mission constructed using Cessna 208 Caravan flight manual [19].

3. Methods

At high altitudes, the ambient pressure drops; hence, the operation of fuel cells requires additional components, starting with a compressor to provide airflow at required pressure. Using the approach of turbocharging, we propose to drive the compressor with a turbine, which, in turn, will run on flue gases from an H_2-combustor. The power requirement for the aircraft mission, presented in Fig. 1, will be delivered solely by the work of PEM-FCs assembled in stacks. Because PEM-FCs work at 60-80ºC, the required flows of compressed air and H_2 need to be cooled and heated, respectively. Moreover, to keep the PEM humidified, the moisture content should be managed. Summarising the above requirements, the FCPS proposed here will comprise PEM-FCs, a turbocharger with a heat exchanger, an air humidifier, and a combustor. To decide on the system architecture, component sub-models were constructed in MATLAB and linked to form a complete FCPS model. Though these are lumped models, reference to commercially available equipment was prioritised where available. Based on the simulation results, an optimised FCPS architecture is proposed and presented in Section 4.

3.1. PEM-FC model

Electrochemical principles and thermodynamics were used to build the core of a PEM-FC model, later including typical empirical constants and correlations taken from the literature. The following assumptions were made:

1. The modelled FC stacks operate at moderate and constant pressures ($1-2$ bar; all pressures discussed in the manuscript are absolute) and temperatures ($60-80$°C); hence, the ideal gas behaviour remains valid.
2. Negligible pressure drop across the stack and no pressure gradient between the FC electrodes were assumed.
3. The thermal architecture was not modelled; it was assumed that the FC stacks include an optimised, prefabricated cooling system (*e.g.* as offered by FC stack manufacturers [21, 22]). Negligible energy requirement for the cooling system was also assumed as justified by the results of Han *et al.* [23].
4. Membranes water activity (λ), a parameter that governs ohmic losses, was assumed to depend solely on the relative humidity (RH) of air at the cathode as per Toyota MIRAI's stack system without self-humidification [24] discussed and analysed by Liu *et al.* [25]. The water concentration gradient formed between the cathode and anode was assumed sufficient to maintain a uniform λ across the membrane, leaving the H_2 at the anode side essentially dry.
5. The chemical activity of the product, liquid water, was taken as unity. Efficiency calculations for the fuel cells were based on the high heating value of H_2 ($\mathrm{HHV}_{\mathrm{H_2}}$). For the combustor, the calculations were performed using the low heating value ($\mathrm{LHV}_{\mathrm{H_2}}$) to simulate a physically realistic outcome (no liquefication of H_2O from combustion off-gases). Previously published studies with turbocharged PEM-FC for aviation reported results based on $\mathrm{LHV}_{\mathrm{H_2}}$ and $\mathrm{HHV}_{\mathrm{H_2}}$ ([11, 12]). Hence, care should be taken when comparing efficiencies.

A single PEM fuel cell is an electrochemical cell, which converts chemical energy into electricity through redox reactions:

$$\mathrm{H_2(g)} + \frac{1}{2}\mathrm{O_2(g)} \rightarrow \mathrm{H_2O(l)} \tag{1}$$

$$\text{Anode:} \qquad \mathrm{H_2(g)} \rightarrow 2\mathrm{H^+(aq)} + 2\mathrm{e^-} \tag{2}$$

$$\text{Cathode:} \qquad \frac{1}{2}\mathrm{O_2(g)} + 2\mathrm{H^+(aq)} + 2\mathrm{e^-} \rightarrow \mathrm{H_2O(l)} \tag{3}$$

The open-circuit voltage (E_{oc}) is the maximum potential that can be produced by a given cell when there is no load connected. The temperature and pressure dependency of E_{oc} can be calculated using the Nernst equation [23].

$$E_{oc} = E_o - 8.5 \times 10^{-4}(T_{stack} - 298.15\ K) + \frac{RT_{stack}}{2F}\ln\left(\frac{p_{H_2}.p_{O_2}^{0.5}}{1}\right) \tag{4}$$

where, E_o is the $H_2|O_2$ redox Standard Potential (1.229 V), R is the universal gas constant, T_{stack} is the stack operating temperature, F is the Faraday constant (96,485 C/mol), p_{H_2} is the partial pressure of H_2, and p_{O_2} is the partial pressure of O_2. Details on the Nernst equation and the origin of the -8.5×10^{-4} constant are given in the Supplementary Material, Section A.

In FC operations, energy losses fall into three categories with magnitudes varying with the current load; these are (1) activation, V_{act}, (2) ohmic, V_{ohmic}, and (3) concentration, V_{conc}, overpotentials:

$$V_{cell} = E_{oc} - V_{act} - V_{ohmic} - V_{conc} \tag{5}$$

The activation overpotential, V_{act}, arises at both electrodes:

$$V_{act} = V_{act,@anode} + V_{act,@cathode} \tag{6}$$

and can be calculated as:

$$V_{act,@anode} = \frac{RT_{stack}}{2\alpha_{anode}F}\ln\left(\frac{i_{load}+i_n}{i_{0,anode}}\right) \tag{7}$$

$$V_{act,@cathode} = \frac{RT_{stack}}{2\alpha_{cathode}F}\ln\left(\frac{i_{load}+i_n}{i_{0,cathode}}\right) \tag{8}$$

where, α_{anode} is the charge transfer coefficient at the anode, i_n is the internal current density, $i_{0,anode}$ is the exchange current density at the anode, $\alpha_{cathode}$ is the charge transfer coefficient at the cathode, and $i_{0,cathode}$ is the exchange current density at the cathode.

Activation losses are related to the kinetics of the electrochemical reactions and the charge transfer at the surface of the electrodes or catalyst layer [26]. The exchange current density at a given electrode then depends on the temperature and catalyst specifications [3]:

$$i_{0,anode} = \gamma_{rf}\exp\left[-\frac{\Delta G_{act,anode}}{R}\left(\frac{1}{T_{stack}}-\frac{1}{T_{ref}}\right)\right] i_{0,anode}^{ref} \tag{9}$$

$$i_{0,cathode} = \gamma_{rf}\exp\left[-\frac{\Delta G_{act,cathode}}{R}\left(\frac{1}{T_{stack}}-\frac{1}{T_{ref}}\right)\right] i_{0,cathode}^{ref} \tag{10}$$

where, γ_{rf} is the electrode roughness factor, $\Delta G_{act,anode}$ is the Gibbs free energy of activation at the anode, $i_{0,anode}^{ref}$ denotes the reference $i_{0,anode}$, then, T_{ref} is the reference temperature (298.15 K), $\Delta G_{act,cathode}$ is the Gibbs free energy of activation at the cathode, and $i_{0,cathode}^{ref}$ denotes the reference $i_{0,cathode}$.

The ohmic overpotential (V_{ohmic}) arises from the internal electrical resistance in the FC stack, *i.e.* the resistance of materials used for the electrical circuitry, and, more significant, ionic losses in the membrane [26] which, in turn, depend on the humidification of the membrane and its thickness;

$$V_{ohmic} = R_{ionic,mem} I = \frac{\delta_{mem}}{A\sigma_{mem}} I = \frac{\delta_{mem}}{\sigma_{mem}} i_{load} \tag{11}$$

where, $R_{ionic,mem}$ is the resistance of the membrane, I is the load current, δ_{mem} is the membrane thickness (taken as 0.0183 cm, Nafion 117 [5]), σ_{mem} is the membrane conductivity.

In Eq. (11), σ_{mem} was calculated using an empirical expression for Nafion-based membranes [5], [6]:

$$\sigma_{mem}\ (\Omega^{-1} cm^{-1}) = (0.005139\lambda - 0.00326) \exp\left[1268\left(\frac{1}{303K} - \frac{1}{T_{stack}}\right)\right] \tag{12}$$

with

$$\begin{array}{ll} \lambda = 0.043 + 17.18(RH) - 39.85(RH^2) + 36.0(RH^3) & RH \leq 1 \\ \lambda = 14 + 14(RH - 1) & 1 < RH \leq 3 \end{array} \tag{13}$$

The RH was calculated based on the water content at the cathode fed with humid air and the saturation pressure of water at the operating temperature. The RH calculations accounted for the H_2O formation from the redox reaction, arriving at the final RH by taking the logarithmic average between the outlet and inlet as proposed by Lazar *et al*. [27].

Concentration overpotential (V_{conc}) is caused by the local depletion of reactants near the electrodes. This loss occurs at high power draws when the generation of current becomes limited by the rate of mass transfer of the reactants.

$$V_{conc} = -\frac{RT_{stack}}{2F} \ln\left(1 - \frac{i_{load}}{i_L}\right) \tag{14}$$

where, i_L is the limiting current density.

Accounting for the influence of the described losses, typical operating cell voltages for PEM-FC are in the range of 0.6-0.7 V, though some systems work up to 0.8 V [28]. Thangavelautham [29] showed an exponential drop in the cell lifetime operating above 0.8 V. Thus, the FC operation considered here was mostly limited to the Ohmic region, with current densities between 0.3 – 1.0 A/cm^2. The parameters used in the PEM-FC model are summarised in Table **1**.

Table 1 Empirical parameters used in the PEM-FC Model.

Parameters	Typical range	Values used in the model
$\boldsymbol{\alpha_{anode}}$	0-1, usually approximated as 0.5	0.35 to match with Ref. [6]
$\boldsymbol{\alpha_{cathode}}$	0-1, usually approximated as 0.5	0.85 to match with Ref. [6]
$\boldsymbol{\Delta G_{act,anode}}$	18 kJ mol^{-1} [30] to 30 kJ mol^{-1} [31]	29 kJ mol^{-1}[6]
$\boldsymbol{\Delta G_{act,cathode}}$	56 kJ · mol^{-1} [32] to 76 kJ · mol^{-1} [30]	66 kJ mol^{-1}[6]
$\boldsymbol{i_n}$	Could be taken as membrane to be electronically insulating	0
$\boldsymbol{i_{0,anode}^{ref}}$	$10^{-4} - 10^{-3}$ A · cm^{-2} [33]	10^{-4} A cm^{-2}[6]

$i_{0,cathode}^{ref}$	10^{-9} – 10^{-8} A · cm^{-2} [33]	10^{-9} A cm^{-2}[6]
γ_{rf}	20-90 [34]	47 to match with Ref. [6]
δ_{mem}	0.0022 – 0.0254 cm [35]. Mark V FC contains Nafion 117 at 0.0183 cm	0.0183 cm [5]
i_L	0.5 – 1.5 Acm^{-2} [36] or >2 [37]	1.5 Acm^{-2}[5]

Power (Pow) achieved from an FC-stack for a given load:

$$Pow = V_{cell} \times N_{cell} \times i_{load} \times A_{cell} = V_{cell} \times I \times N_{cell} \quad (15)$$

where N_{cell} is the number of cells and A_{cell} is the cell area; both taken from stack's specifications (*i.e.* Ballard's Mark V, 5 kW stack with $N_{cell} = 35$, $A_{cell} = 232\ cm^2$ [5]). The stack design was scaled for larger stack sizes, looking at the powers and sizes of commercially available modules. For example, the power output was modelled for two commercial stacks of different sizes with a known number of cells and cell area, and another two with no such specifications but with characteristics available from the literature. Specifically, 85 kW and 21 kW stacks were modelled using their actual N_{cell} and A_{cell} found in the literature [38, 39], while 100 kW and 30 kW stacks were modelled by scaling Ballard's Mark V, 5 kW stack (*e.g.* $N_{cell,100kW} = 100\ kW \div 5\ kW \times 35_{(N_{cell,5kW})} = 700$). Figure 2.a) shows that both methods led to accurate estimation of stacks' power output. The Fuel-Cell model was further validated against experimental results [2] for a Ballard Mark V, 5 kW stack, operated at 70℃ and 3 atm. The results are presented in Fig. 2.b), showing only a slight overshoot of the model at high current densities. In the expected operating region (Ohmic at 0.3 – 1.0 A/cm^2), the agreement between the published results and constructed model was satisfactory.

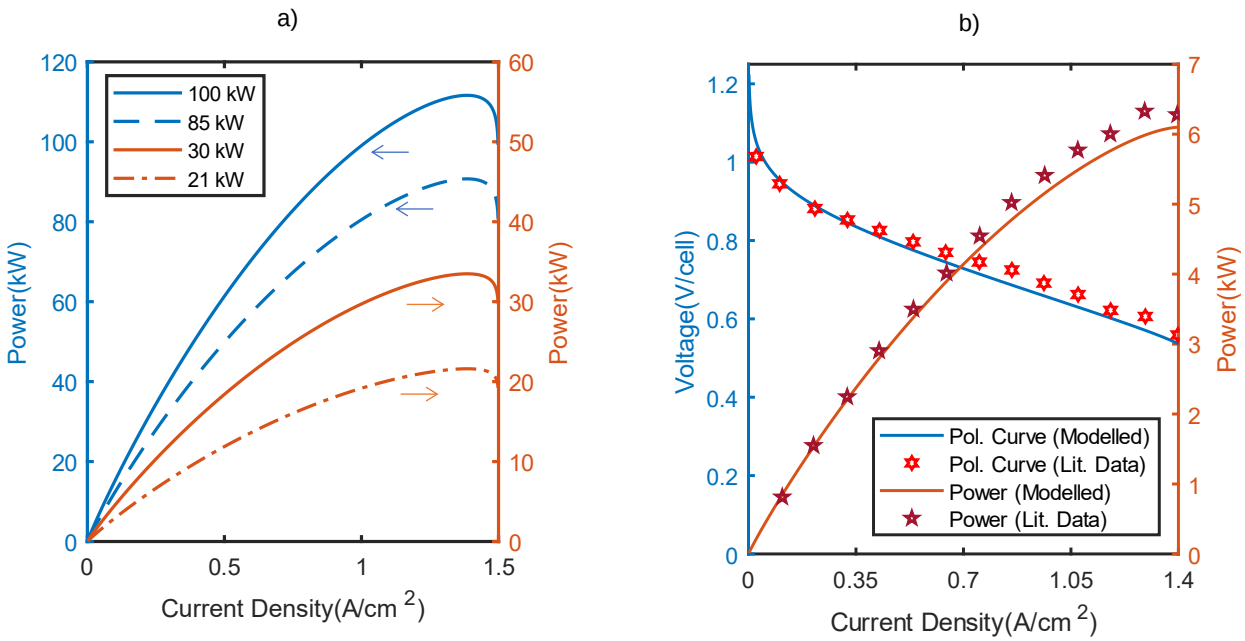

Figure 2. a) Power output of differently sized FC-stacks, modelled for 21 kW, 30 kW, 85 kW, and 100 kW; b) Comparison between modelled polarisation and power output curves with published experimental results for Ballard Mark V stack [5].

Mass flows of reactants during power draw was calculated following Larmanie *et al.* [40].

$$\dot{m}_{H_2,FC}(kgs^{-1}) = \left(1.05 \times 10^{-8} \frac{Pow}{V_{cell}}\right) \tag{16}$$

$$\dot{m}_{Air,FC}(kgs^{-1}) = \left(35.7 \times 10^{-8} \frac{P}{V_{cell}}\right) \tag{17}$$

Note that Eqs. (16) and (17) assume stoichiometric amounts of reagents in the redox reactions. Typically, PEM-FC operations require some excess amounts of reactants, so a fixed reactant excess factor of 1.6 was employed both for the cathode and anode sides, following [4] and [41].

3.2. Turbocharger Model

The turbocharger model was based on thermodynamic process calculations for compression and expansion [13, 42, 43]. Regardless of the number of stages, the work required by a compressor and work obtained at a turbine can be determined based on the outlet and inlet conditions and isentropic efficiencies, as described in Eqs. (18)-(23):

$$P_{C,out} = P_{R_C} \times P_{C,in} \tag{18}$$

$$T_{C,out} = T_{C,in} + \frac{T_{C,in}}{\eta_C}\left[\left(P_{R_C}\right)^{\frac{\gamma_{air}-1}{\gamma_{air}}} - 1\right] \tag{19}$$

$$\dot{W}_{C,req.} = \frac{c_{p_{air}} \times T_{C,in}}{\eta_C} \times \left[\left(P_{R_C}\right)^{\frac{\gamma_{air}-1}{\gamma_{air}}} - 1\right] \times \dot{m}_{air,C} \tag{20}$$

$$P_{T,out} = \frac{1}{P_{R_T}} \times P_{T,in} \tag{21}$$

$$T_{T,out} = T_{T,in} - T_{T,in} \times \eta_T \left[\left(\frac{1}{P_{R_T}} \right)^{\frac{\gamma_{exh}-1}{\gamma_{exh}}} - 1 \right] \tag{22}$$

$$\dot{W}_{T,obt.} = \eta_T \times c_{p_{exh}} \times T_{T,in} \times \left[1 - \left(\frac{1}{P_{R_T}} \right)^{\frac{\gamma_{exh}-1}{\gamma_{exh}}} \right] \times \dot{m}_{exh,T} \tag{23}$$

where subscripts C and T describe parameters for compressors and turbine, respectively, so a subscript i describes the general form. Hence, $P_{i,in}$ is the inlet pressure, $P_{i,out}$ is the outlet pressure, P_{R_i} is the pressure ratio, $T_{i,in}$ is the inlet temperature, $T_{i,out}$ is the outlet temperature, γ_{air} is the heat capacity ratio for air, $c_{p,air}$ is the specific heat capacity for air, γ_{exh} is the heat capacity ratio for the exhaust gas, $c_{p,exh}$ is the specific heat capacity for the exhaust flow, η_i is the isentropic efficiency, $\dot{W}_{C,req.}$ is the work required by the compressor, $\dot{W}_{T,obt.}$ is the work produced by the turbine, $\dot{m}_{air,C}$ is the mass flowrate of compressed air, $\dot{m}_{exh,T}$ is the mass flowrate of the turbine exhaust.

In a turbocharger, compressor and turbine are connected with a shaft. The mechanical loss in the work transmitted from the turbine to the compressor was taken as 10% [13], leading to a requirement for matching both types of work: $\dot{W}_{C,req.}/0.9 = \dot{W}_{T,obt.}$. For simplicity, the calculations used fixed values of η_i, assuming that the compressor and turbine operated at the desired pressure ratios with the fixed efficiency regardless of the fluid mass flow. Specifically, η_C and η_T were set as 75% [13] with high excess fluid flowrates (1.8 to 2.2 times the minimum air requirement determined in Eq. (17)). This assumption is more suitable for turbines since they often work at a fixed maximum efficiency [44]. However, for compressors, the efficiency depends on the pressure ratio, P_{R_C}, and the air flowrate, $\dot{m}_{air,Comp}$, presented in compressor maps [44]. Therefore, to justify the assumed efficiency for compression, a commercially available turbocharger was selected, namely the G25-550 turbocharger by Garrett [44], checking the operability range and the power requirements arising from the modelled FCPS during the proposed mission.

3.3. Heat Exchanger Model

Any PEM-FC applications with LH2 require fuel preheating since the storage tanks release $H_{2(g)}$ at cryogenic temperatures (<-250℃), and cooling of air, which after compression is usually at a much higher temperature than the operating range in PEM-FC. Hence a heat exchanger is proposed. With a fixed 5 kPa pressure drop imposed, the heat exchanger model was primarily based on heat transfer principles. The calculations were performed assuming perfect heat transfer from the heat source, the hot compressed air, to the cold H_2, accounting for the H_2 enthalpy change. Thermal properties were taken from the NIST database [45];

$$T_{hotout} = \frac{-\left(\Delta\widehat{H}_{H_2,out} - \Delta\widehat{H}_{H_2,in}\right) \times \dot{m}_{H_2,FC}}{\dot{m}_{air,C} \times c_{p,air}} + T_{hot,in} \quad (24)$$

where, $T_{hot,in}$is the inlet temperature of the hot medium (compressed air), $T_{hot,out}$ is the outlet temperature of the hot medium (compressed air), $\Delta\widehat{H}_{H_2,in}$is the specific enthalpy of H_2 entering the preheater, $\Delta\widehat{H}_{H_2,out}$ is the specific enthalpy of H_2 exiting the preheater.

The effectiveness-Number of Transfer Units (e-NTU) method [46] was used to provide sizing estimates for a gas-to-gas cross flow heat exchanger.

$$C = \frac{\min\left(\dot{m}_{hot} \times c_{p,air} | \dot{m}_{H_2,FC} \times c_{p,H_2}\right)}{\max\left(\dot{m}_{hot} \times c_{p,air} | \dot{m}_{H_2,FC} \times c_{p,H_2}\right)} \quad (25)$$

$$NTU = \frac{UA_{HT}}{\min\left(\dot{m}_{hot} \times c_{p,air} | \dot{m}_{H_2,FC} \times c_{p,H_2}\right)} \quad (26)$$

$$\epsilon = 1 - \exp\left[\frac{\exp[-NTU \times C \times (NTU^{-0.22})] - 1}{C \times (NTU^{-0.22})}\right] \quad (27)$$

$$Q_{actual} = \epsilon \times \left[\min\left(\dot{m}_{hot} \times c_{p,air} | \dot{m}_{H_2,FC} \times c_{p,H_2}\right)\right] \times \left(T_{hot,in} - T_{H_2,in}\right) \quad (28)$$

$$T_{hot,out} = T_{hot,in} - \frac{Q_{act}}{\dot{m}_{hot} c_{p,air}} \quad (29)$$

$$T_{H_2,out} = T_{H_2,in} + \frac{Q_{act}}{\dot{m}_{H_2,FC} c_{p,H_2}} \quad (30)$$

where, c_{p,H_2} is the specific heat capacity of H_2, U is the overall heat transfer coefficient, taken as 20 $\mathrm{W\,m^{-2}\,K^{-1}}$, so at the midpoint for U expected in gas-to-gas heat changers [47]. Then, A_{HT} is the heat transfer area, Q_{actual} is the actual heat transfer at the intercooler, $T_{H_2,in}$ is the inlet temperature of the H_2 side, $T_{H_2,out}$ is the outlet temperature of the H_2 side, $T_{hot,in}$ is the inlet temperature of the hot side, $T_{hot,out}$ is the outlet temperature of the hot side.

During calculations, the value for A_{HT} was iterated to achieve $T_{H_2,out} = T_{stack}(\pm 0.5℃)$. Details of the e-NTU method and an example of performed calculations are given in the Supplementary Material, Section B.

3.4. Water Management and the Humidifier Model

During the operation of PEM-FC, water is created, but it leaves the stack with the flowing gases. As presented in Eq. (11), the efficiency of the PEM-fuel cell depends on the moisture content in the membrane. To keep the membrane humid at all times, the airflow prior to the fuel cell is usually humidified by injecting water or by taking the water from the waste humid air stream after the fuel cell. The second approach is preferred in aviation, avoiding additional ballast of liquid water at the cost of an additional unit for air humidification.

In the proposed humidifier, the moisture is exchanged based on the RH difference between the wet (waste air) and dry (fresh air) sides of the humidifier. Here, the inlet and outlet conditions were known *a priori* due to the set humidification goal. For instance, at 100 kW_{el} power draw under mid-operating conditions (70°C and 1.5 bar), to achieve a log mean cathode side RH of 100% and taking the amount of water formed through the redox reactions into consideration, the cathode side inlet and outlet RH would be 65% and 145%, respectively. At 100 kW_{el}, the amount of water needed to reach 65% RH from 0% RH was calculated as ~32 kg/h, which was less than the amount of water formed (~45 kg/h), suggesting sufficient levels of water in the system. Thus, the humidifier can be operated with the dry side's inlet and outlet moisture levels of 0% RH and 65% RH, respectively, and the wet side's inlet and outlet moisture levels of 145% and 100% RH, respectively. Here, the RH levels beyond 100% indicate liquid water, which then evaporates in the humidifier; hence, the overall energy balance for the waste air stream (wet side) remains unchanged.

The humidifier model was constructed to verify that the moisture exchange was within achievable limits. Park *et al.* [48] analysed dynamic and static behaviours of a Perma Pure [49] humidifier designed for 80 kW FC stacks. Following their governing equations for the moisture exchange, the humidifier unit can be scaled and adapted. The rate of water transfer, $\dot{m}_{H_2O,trans}$, from humidifier's wet to dry side is:

$$\dot{m}_{H_2O,trans}(\mathrm{kg\ s^{-1}}) = D_w \frac{C_{w,shell} - C_{w,tube}}{mem_{thick}} M_{w,H_2O} A_{WT} \tag{31}$$

where, D_w is the membrane's water diffusion coefficient, $C_{w,shell}$ is the water concentration at shell side, $C_{w,tube}$ is the water concentration at tube side, $\delta_{mem,tube}$ is the membrane tube thickness (75 μm), A_{WT} is the membrane's water transfer area.

Note that the humidifier specified by Park *et al.* [48] comprised 10,000 Nafion-based tubes with 0.94 mm inner diameter (all enclosed in 0.19 m diameter housing) and 0.267 m length. The water diffusion coefficient was then calculated using empirical correlations:

$$D_w(cm^2 s^{-1}) = D_\lambda \exp\left[2416\left(\frac{1}{303} - \frac{1}{T_{mem}}\right)\right] \tag{32}$$

with:

$$D_\lambda = \begin{cases} 10^{-6} & \lambda_{mean} < 2 \\ 10^{-6}[1 + 2(\lambda_{mean} - 2)] & 2 \le \lambda_{mean} \le 3 \\ 10^{-6}[3 - 1.67(\lambda_{mean} - 3)] & 3 < \lambda_{mean} < 4.5 \\ 1.25 \times 10^{-6} & \lambda_{mean} \ge 4.5 \end{cases} \tag{33}$$

and membrane average temperature (close to T_{stack} as established):

$$T_{mem} = \frac{T_{exh,inlet} + T_{wet,outlet}}{2} \tag{34}$$

where, D_λ is the empirical constant for D_w relationship, T_{mem} is the membrane temperature, $T_{exh,inlet}$ is the FC stack exhaust temperature, $T_{wet,outlet}$ is the humidified gas outlet temperature, λ_{mean} is the average water activity between shell and tube side.

Here, λ_{mean} was determined from Eq. (13) as PEM-FC and Perma Pure humidifiers use Nafion™ based membranes. Following that, C_w could hence be computed before calculating the water transfer rate at the humidifier.

$$C_{w,shell} = \frac{\rho_{mem,dry}}{M_{equiv,dry}} \lambda_{shell} \tag{35}$$

$$C_{w,tube} = \frac{\rho_{mem,dry}}{M_{equiv,dry}} \lambda_{tube} \tag{36}$$

where, $\rho_{mem,dry}$ is the membrane's dry density (0.001 $kgcm^{-3}$), $M_{equiv,dry}$ is the membrane's dry equivalent weight (1.0 $kgmol^{-1}$), λ_{shell} is the shell side's water activity of the membrane, λ_{tube} is the tube side's water activity of the membrane. For the maximum power draw required, up to seven identical humidifier units would be needed (560 kW ÷ 80 kW = 7). However, it is most likely that larger, custom-designed humidifier units can be designed, enlarging the length and shell diameter to fit in a larger number of tubes per humidifier.

3.5. Combustor Model

Turbocharger applications in PEM-FC systems are constrained by low exhaust temperatures from the FC stacks, leading to low turbine inlet temperatures. A combustor is therefore needed to raise the temperature of the exhaust gas used to power the turbine. Several possibilities for combustors include a flame type combustor, spark-ignition engine, or catalytic combustor. Here, a simplified combustion model is used to determine the outlet temperature, noting however that H_2 combustion is more complex and commends its own separate analysis. Here, the temperature at the combustor outlet was calculated as:

$$T_{comb,out} = \frac{\dot{m}_{fuel} \times LHV_{H_2} \times \eta_{comb}}{\dot{m}_{exh} \times c_{p_{exh}}} + T_{comb,in} \tag{37}$$

where, $T_{comb,out}$ is the combustor outlet temperature, $T_{comb,in}$ is the combustor inlet temperature, $\dot{m}_{fuel}$ is the mass flowrate of H_2 fed into the combustor, η_{comb} is the combustion efficiency, $\dot{m}_{exh}$ is the mass flowrate of exhaust exiting the combustor.

Almost complete combustion was assumed ($\eta_{comb} = 0.98$ [50]). In Eq. (37), $\dot{m}_{ex}$, $c_{p_{exh}}$, and $T_{comb,out}$ are interdependent, hence, were computed iteratively.

Knowing the amount of H_2 used in the FC and combustor, the overall FCPS efficiency (η_{eff}) was determined as

$$\eta_{eff} = \frac{P}{HHV_{H_2}\left(\dot{m}_{H_2,FC} + \dot{m}_{fuel}\right)} \times 100\% \tag{38}$$

A summary table of the components model, references sourced, and approaches used for validation is provided in the Supplementary Material (Section C).

4. Results and discussion

4.1. Architecture Design

Figures 3 and 4 illustrate the fluidic architecture of FCPS, selected after optimising the system's performance during the proposed mission when looking for the highest system efficiency and the lowest consumption of LH2.

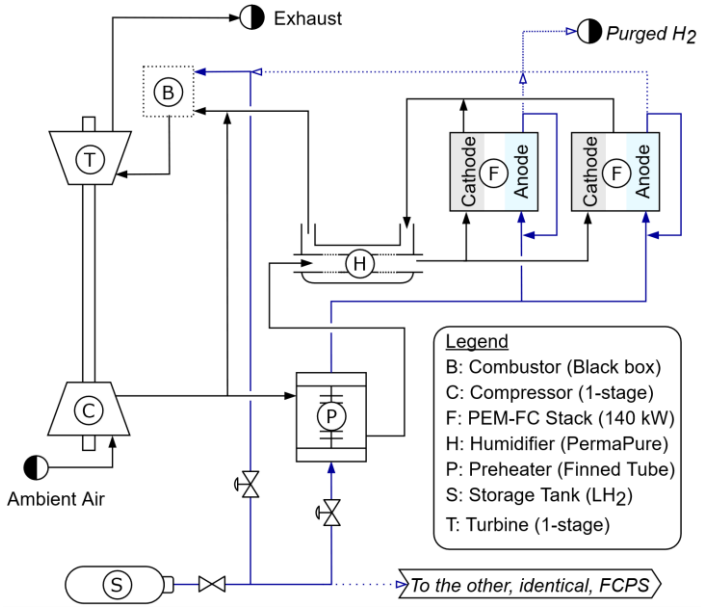

Figure 3. Proposed turbocharged FCPS for the Cessna 208 Caravan retrofit shown for one side of the system and is to be repeated for the remaining side.

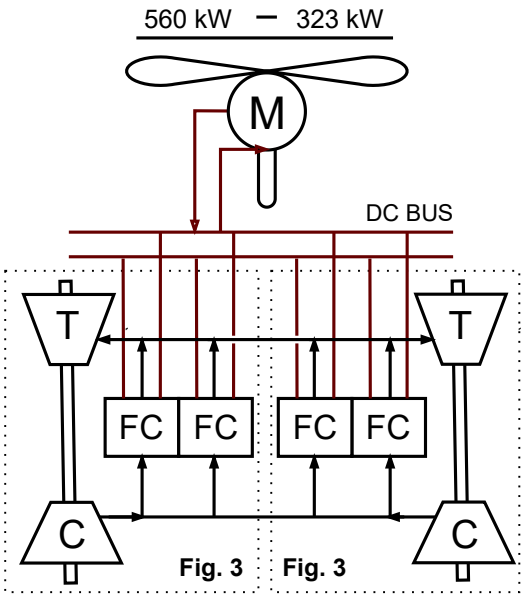

Figure 4. Overall architecture showing Fuel Cell stacks (FC) and turbocharger blocks (C: Compressor, T: Turbine), the fluid flow for the Air-side as well as electric connections to propellers (M: Motor for applications in Magni-500 based electric propeller). Figure 3 is simplified to the FC stacks and turbocharger (dotted box) and appears twice to present the "dual" FCPS.

In Fig. 3, LH_2 from the storage tank (S) gives off H_2 gas at <-250℃, substantially below the operating temperature of FC stacks. As shown in Fig. 3, H_2 for the combustor (B) is not preheated, similarly to the LH2-powered system proposed by Atreya *et al.* [12]. In consequence, a portion of the combustion energy is used for preheating already in the combustor. Experiments by Panda and Hecht [51] presented such cryogenic combustion of H_2 without the need for preheating. Here, however, two additional flows to the combustor: waste air and waste H_2 after the FC stacks contain moisture; hence, potentially, the whole H_2 feed may need to be ≥ 5℃ to prevent issues with water freezing. For the simplicity of the proposed FCPS, we assume that all inlet streams mix well, and the freezing of water can be ignored.

For heating of the H_2 feed directed to the stacks, two heat sources are identified: the hot compressed air from the compressor (C) or a portion of the exhaust gas from the combustor outlet (B). Because of the low density, the low-pressure exhaust after the turbine (T) is excluded; its usage would require excessively large heat exchangers, as

discussed in [13]. From the considered two options, the hot compressed air is preferred because this stream itself requires cooling before entering the PEM-FC. In the third alternative scenario, rerouting the combustor exhaust for H_2 heating would increase fuel consumption because less heat would be available for the turbine. In Fig. 3, the heat exchange between the cold H_2 stream and the hot air stream is carried out in a preheater (P).

After assessing the variation of the ambient pressure during the mission, it was determined that a single-stage compressor is needed. As shown in Fig. 3, the airflow after the compressor (C) is split into two streams: the air entering the FC stacks and a possible system bypass. The bypass is required to avoid the compressor surge when the power draw is low. Moreover, by passing a fraction of the compressed air stream, the sizing requirements of the air-to-H_2 heat exchanger and humidifier depended only on the airflow requirements in the FC-stacks. Because the compressor is allowed to draw more air than needed to operate the FC stacks, the drawn mass flowrate of air is calculated as $\dot{m}_{air,Comp} = \left(1.6 + F_{byp}\right) \times \dot{m}_{Air,FC(stoich)}$, where 1.6 represents the excess factor in the FCs (see Section 3.1), while F_{byp} is the bypass factor relative to the stoichiometric air requirement. Flows of the bypassed, compressed air, and the cooled waste air after the stacks are directed to the combustor.

The H_2 flow through the anode side in the FC stacks is also higher than required in the FC operation, recirculating the unreacted H_2 back to the FC. Alternatively, a fraction of the unreacted H_2 is directed from the anode to the combustor. However, the main H_2 feed to the combustor is independent of the FC to create a more reliable, unconstrained feeding system. To prevent possible water and nitrogen build-up at the anode, a purge line is also proposed. Water management for maintaining the proper stack humidification is achieved by using the water produced in the $H_2|O_2$ redox reaction on the cathode side (Assumption No. 4). The water is then recycled using a humidifier (see Section 3.4), thus, the water management configuration avoids additional tanks for on-board water storage.

For selecting appropriate FC-stacks, large power requirements could be met with multiple smaller stacks instead of a single stack sized to the max load. Ballard's approach in combining 24 stacks of Mark Vs for their FC powered bus is an example [52]. To apply a similar approach for the system discussed here, the largest PEM-FC stack offered by Ballard for transportation applications is used, namely, their FCgen®-HPS, rated at 140 kW [53]. A multi-stack system with four 140 kW FC stacks is needed to meet the power requirements for propulsion outlined in Section 2 (Fig. 1) and allow one stack redundancy. As shown in Fig. 4, it is proposed to split the load into two identical FCPS systems (duplicates of the FCPS in Fig. 3), each with $2\times$ FCgen®-HPS units, a dedicated LH_2 storage tank, and an air-subsystem. The two FCPS are connected on the Air and H_2 sides, allowing each system to take reactants from the other. The overall system would, thus, have redundancies in place for each core component. Following that, parallel fluidic and electrical connections architectures are chosen because of the highest achievable net power output and the

option for quick isolation of inactive or failed stacks as stated by Cardozo *et al.* [54] and Marx *et al.* [55]. Adding off-the-shelf “Cell Bypass Switches” [56] between the stacks and the DC Bus is also proposed, aiming to isolate failed stacks and avoid short circuit. The resulting parallel arrangement is shown in Fig. 5. Note that even if a larger PEM-FC stack rated at 280 kW_{el} were commercially available and the multi-stack architecture reduced to two 280 kW_{el} stacks, the quadruple 140 kW_{el} architecture would still be preferred as the design should account for risk management and load delegation. If a two stacks failure were to occur, the 2×280 kW_{el} system would experience a complete power loss, but such events occurring in a 4×140 kW_{el} system would still have 280 kW_{el} power remaining.

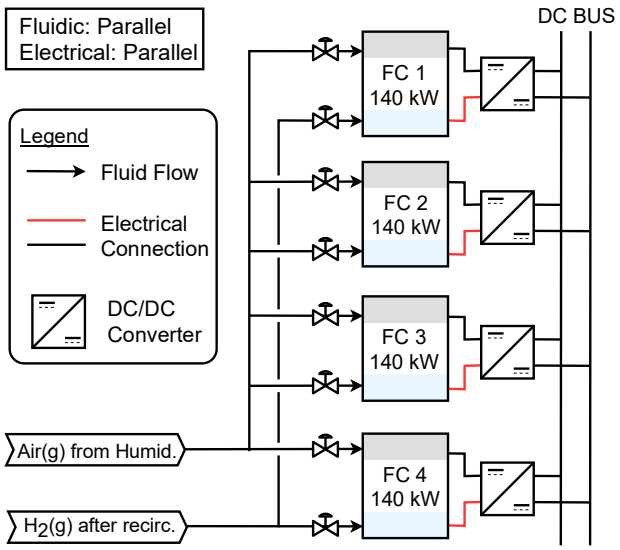

Figure 5. Multi-stack architecture with parallel electrical and fluidic connections. Outlet fluid flows not shown to improve visual clarity.

To summarise, the identified equipment involved in the proposed architecture as illustrated in Figs. 3 – 5 comprise four FC-Stack units (potential product: Ballard FCgen®-HPS 140 kW stacks but other types of FC-stacks and new-type FC-products might be more suitable for aviation); two turbochargers (potential product: Garrett G25-550); two preheaters (bespoke Air-to-H_2 heat exchanger, potentially also by Garett with their cooler/heat exchanger product line [44]); two humidifiers (bespoke unit by Perma Pure); two LH2 storage tanks. Note that material compatibility should also be taken into account to prevent operational issues caused by, for example, ion-contamination or hydrogen embrittlement.

The architecture design for the FCPS requires several practical considerations. For modelling of the chosen 140 kW stack, a scaling procedure described in Section 3.1 is performed. A turbocharger is selected by analysing compressor maps of commercially available equipment [44]. The proposed Garrett’s G25-550 can reach pressure ratios and efficiency ranging between 1.25 – 3.75 and 68% – 80%, respectively. This compression capability is sufficient to feed air to the FC stacks, taking that P_{amb} drops with altitude down to ~0.7 bar (3.05 km). Considering the stack’s operating pressure is taken to be at most 2 bars, the maximum required pressure ratio would be ~3, hence, safely within the

compressor's operating range. The estimated required heat transfer area during cruising was $A_{HT} \approx 7.34$ m^2; hence it is used to size the heat exchanger. For the humidifiers, the calculated rates of water transfer are compared to the performance of a Perma Pure unit for 80 kW_{el} power draw used by Park *et al.* [48]. The water transfer in the Perma Pure unit is, however, reassessed for the RH differences expected for our system (dry side of 0% → 65% RH, wet side of 145% RH→ 100% RH as described in Section 3.4), giving water flowrates 20 – 30% higher than the water transfer required in our FCPS. If the assessed flowrates were instead smaller, larger or multiple humidifier units would have been required. The inclusion of a combustor is proposed to produce flue gas for driving the turbine; however, H_2 combustion with air could signify a risk for NO_x emission. The NO_X formation can be minimised by decreasing the combustion temperature, for example, when the process is carried out with excess air and near the lower flammability limit of 4.0%vol [57]. Nevertheless, the risk of NO_x creation means potential greenhouse gas emissions, even though the system is carbon-free.

4.2. Steady-state Responses Across Flight Mission

The constructed FCPS model is used to simulate the flight mission (Fig. 1) with FC-stacks run at $70℃$ and 1.5 bars, with simplified turbocharging calculations (F_{byp} of 0.2, fixed η_c and η_t as discussed in Section 3.2) and with perfect heat exchange in the heat exchanger (Section 3.3). The simulations informe about the overall system efficiency and the H_2 consumption in the FC stacks (140 kW ×4) and the combustor. Throughout the mission, the power requirements shown in Fig. 1 are either split equally among the stacks (case 1, equal distribution mode) or a single stack deactivation is allowed at the end of the climb phase (case 2, daisy-chaining the stacks). Results from both cases are presented in Fig. 6.

The observed trends for η_{eff} and H_2 consumption are affected by the changing ambient conditions with altitude. Ambient pressure decreases with increasing altitude [58], which causes η_{eff} to decrease due to the rising total pressure ratio and so the workload during the air compression. However, the compression workload also depends on the air temperature, which also decreases with altitude, reducing the required work, and thus, the H_2 consumption. The net effect is reflected in Fig. 6 during the climb and descent phases. Figure 6.a) also shows that, to complete the mission, a total of 41 kg of H_2 fuel would be needed for case 1 with equal distribution power-sharing.

As shown in Fig. 1, the required cruising power is 390 kW_{el}. Hence, the proposed architecture comprises 140 kW $\times$ 4 FC stacks: 3 stacks to reach the power requirements, and an additional 4th stack for redundancy. In case 1, with equal power distribution, the power draw from each stack is 97.5 kW. However, the cruising power requirement of 390 kW_{el} is sufficiently low to operate with only three stacks (140 kW $\times$ 3) while deactivating the fourth one. Hence in case 2,

each of the three working stacks would then be operated at 130 kW during cruise, and the fourth one would be left unused, as expected in a daisy-chained power-sharing mode [54].

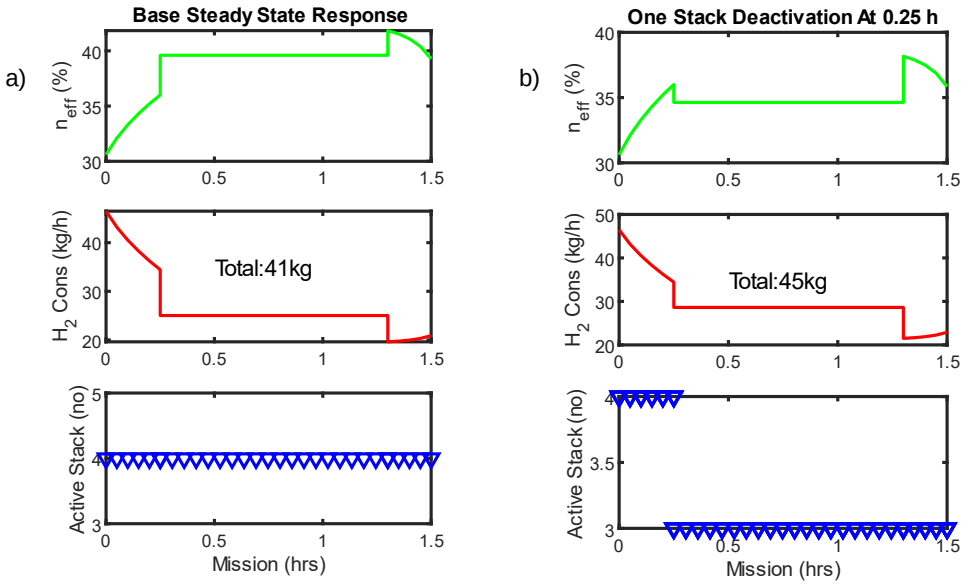

Figure 6. a) Steady State Response of the FCPS under Equal Distribution Power Sharing Mode (case 1) for the Flight Mission constructed; b) A Single Stack deactivation (case 2) when the aircraft reaches its cruising altitude.

A daisy-chained or a sequential power-sharing mode could be performed to preserve a given FC-stack's lifetime. During operations, FC stacks are subjected to slow degradation, which results in decreasing voltage with lifetime. The expected degradation rate is in micro-volts per operating hour; for example, Cardozo *et al.* [54] stated a value of 5 μV/h. As seen in Fig. 6 b), although this voltage decay is avoided for the deactivated stack in case 2, the remaining active stacks operated at a higher power draw (130 kW_{el}) than the four stacks in case 1 (97.5 kW_{el}). Hence, case 2 is affected by greater inefficiencies due to the rising effect of overpotentials. Figure 6.b) shows that this less optimal operation would result in a ~10% increase in H_2 consumption. Life-cycle analysis is recommended to discern the overall value of performing daisy-chained power-sharing modes in the discussed application. Beyond the stack-saving purposes, case 2 informs on case 1's performance in the event of one-stack failure. Namely, case 2 could be seen as a stack failure occurring at the start of cruising, where the aircraft is still permitted to complete its mission with only three working stacks. Because of the consequent drop in the overall efficiency of the FCPS with 3 stacks, the capacity for the LH_2 storage should be sized to account for the higher fuel requirements.

4.3. Failure Analysis

Failure analysis techniques that have been applied to PEM-FCs include the Failure Mode and Effect Analysis (MEA), Fault Tree Analysis (FTA), and Petri-Net Simulation as discussed by Whitely *et al.* [59] to which the authors also proposed the Petri-Net as their most preferred technique for analysing the PEM-FC stack's component failure (*e.g.*

failure at catalyst layer and bipolar plates), mainly because of the complex and interdependent nature of MEA in PEM-FC stacks. For analysing larger systems, with FC stack and the auxiliary equipment, Fault Tree Analysis (FTA) was applied by Collong *et al.* [60], who studied the overall reliability of the system, accounting for other equipment, *e.g.* H_2 storage tank, relief valves and sensors. Here, an FTA with an Exponential Distribution probabilistic technique and fixed failure rates (in a number of failures per million hours) is applied to analyse the failure rate of the proposed FCPS. The FTA method is chosen as the most adequate to analyse multiple subsystems involved.

The Top Event in a mission of an aircraft is the failure to provide power to the propellers. The result, however, might not necessarily indicate a complete catastrophic failure and harm to passengers because the aircraft could still be able to glide while performing safety manoeuvre [19] and "dead-stick landing" [61]. Lower-level Group Events are based on the FCPS subsystems, categorised as "Failure to Provide H_2 to the system", "Failure to Provide Air to the System", and "FC Stacks module's Remaining Power is less than 390 kW_{el}" (at minimum two stacks failing, which is a more conservative event compared to the complete failure of all four stacks). Any of these events occurring will initiate the Top Event, so an "OR" gate connects these upper-level group events.

In commercial aircraft, a turbofan engine has a failure rate as low as $1\times10^{-6}\,h^{-1}$ [62]. But a more direct comparison would be on turboshafts as it is an engine without any propeller attached (essentially the counterpart to FCPS in this study). Even so, this engine has an in-flight shutdown rate of 1 per 651,126 h [63] or $\sim1.6\times10^{-6}\,h^{-1}$. For the analysed FCPS, most of the failure rates for the basic events exceeds the $\sim1 \times 10^{-6}\,h^{-1}$ target (see Fig. 7). However, the final failure rate is significantly lower than the target value, primarily because of the planned comprehensive redundancies. Indeed, the proposed FCPS offers twin systems, each with a single turbocharger, dedicated storage tank, and 2x140 kW stacks. Since for the Top Event to occur, elements from both systems would need to fail simultaneously, the overall reliability of the FCPS is exponentially improved. The fault tree in Fig. 7 shows that the resulting failure rate for the Top Event is $\sim3 \times 10^{-8}\,h^{-1}$, signifying the potential to comply with airworthiness requirements.

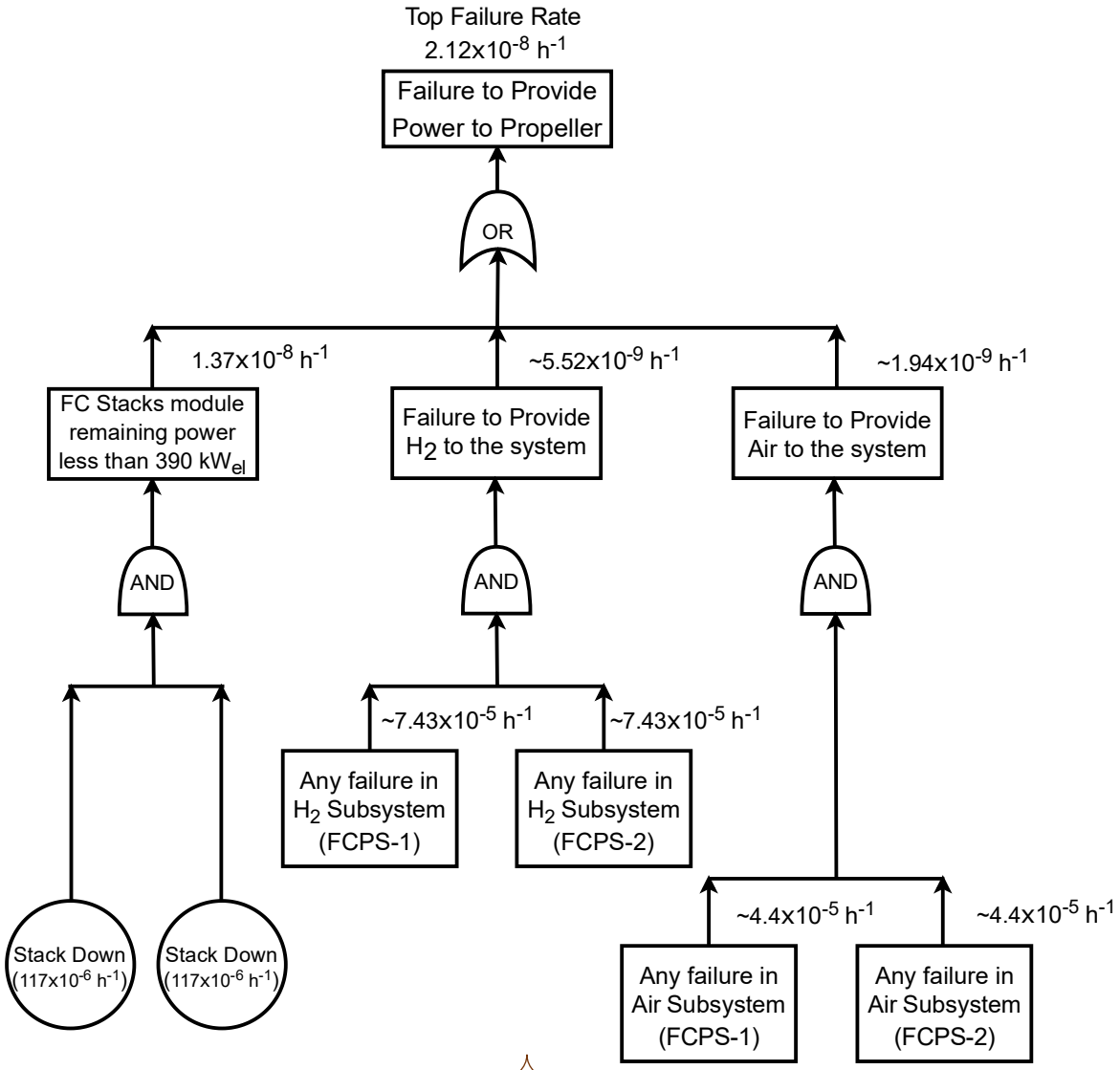

Group Event (Upper Level)	Group/Basic Event Combined (Lower Level)	Basic Events (Bottom Level)	Failure Rate (h^{-1})	Ref.
FC Stack Module's Remaining Power is less than 390 kW	Stack Down	Fuel Cell stack failure (components such as Gas Diffusion Layer, MEA, Gasket, *etc.*) leading to stopping current production	5.5×10^{-5}	[21, 64]
		Controller (Flow) failure to allow correct reactant flow - H_2	3.0×10^{-5}	[65]
		Controller (Flow) failure to allow correct reactant flow - Air	3.0×10^{-5}	[65]
		DC/DC converter failure causing disconnection with DC BUS	2.3×10^{-6}	[66]
Failure to Provide H_2 to the system	Shut-off Valve	Storage Tank's shutoff valve failure blocking H_2 release	3.73×10^{-6}	[60]
	Tank Rupture	Tank spontaneous rupture causing H_2 escaped to atmosphere	1.8×10^{-10}	[60]
	Mains CV (FC Stacks)	Main source control (flow) failure to allow correct flow through valve to provide H_2 to Fuel Cell Stacks	3.0×10^{-5}	[65]
	Blocked H_2 (FC Stacks)	Downstream Preheater blocking H_2 flow	1.0×10^{-9}	[67]
	Mains CV (Combustor)	Main source control (flow) failure to allow correct flow through valve to provide H_2 to Combustors	3.0×10^{-5}	[65]
Failure to Provide Air to the system	Humidifier faults	Blocked/leakage causing no air flow to Fuel Cell Stacks ("Tube")	2.6×10^{-6}	[68]
		Blocked/leakage causing no air flow to combustors ("Shell")	1.0×10^{-8}	[67]
	Combustor Down	Combustor failure causing inability to increase turbine inlet temperature leading to lower to no compression and air intake	1.0×10^{-5}	[69]
	Turbo faults	Compressor failure causing reduced rotation or a complete stop	1.49×10^{-5}	[70]
		Downstream Preheater blocking Air flow	1.0×10^{-9}	[67]
		Turbine failure causing reduced rotation or a complete stop	1.65×10^{-5}	[70]

Figure 7. FTA for Overall FCPS and associated basic events.

4.4. Cessna 208 Caravan FCPS Retrofitting

A study for a potential FCPS retrofit is conducted based on the Cessna 208 Caravan aircraft dimensions and weight specifications. Two major components to be replaced are the original jet fuel and the PT6A-114A jet engine, which could be swapped with the Magni-500 propulsion system like in the eCaravan [17]. Fuel for Cessna 208 Caravan is stored in wings [14] but this storage strategy is currently unfeasible for LH_2, so the LH_2 tanks are placed in the cabin. The cabin compartment presented by Textron Aviation [14] indicates that the space required for the LH_2 tanks and FC-stacks can be created by removing three seats in the back row and two towards the back end of the aircraft; hence, reducing the aircraft occupancy to 8 passengers. The components of the proposed FCPS are not limited to the cabin interior only. For example, the preheater is proposed to be placed outside of the aircraft, while turbochargers near the engine compartment with an in-built exhaust.

At an average passenger weight of 88 kg [71] and with the original usable kerosene storage fuel, the sum of removed weight is estimated as 1273 kg. The corresponding volume available with the removal of the back seats is 4.46 m^3 (2 m long × 1.63 m wide × 1.37 m high). Assuming contemporary gravimetric and volumetric efficiencies of LH_2 tanks of 15% [72] and 45 kg_{H2}/m^3 [73], respectively, which are probably very conservative values of what should be achievable soon, a storage tank for LH_2 with a storage capacity of 60 kg_{H2} (~40% additional margin from the requirements in Fig. 6) is selected. This tank would weigh 400 kg, occupying ~1.34 m^3, capable of providing 60 kg H_2, which is equivalent to ~8.5 GJ energy on a HHV_{H2} basis.

Because of the significant space requirements to fit the LH2 tanks, other options for clean liquid fuels can also be considered. For example, methanol (CH_3OH) can be synthesised from bio-feedstock and used in PEM-FC, with the main benefit arising from the possibility of fuel storage in the aircraft's wings. Assuming a substitute to Direct Methanol Fuel Cells (DMFC), about 370 $kg_{Methanol}$ would be required to replace 60 kg_{H2} because the high heating value of methanol per kg of fuel is only ~16% of that for H_2. However, DMFCs provide lower power density and efficiency than PEMFCs [74]; thus, more stacks will be required, adding weight and taking more space in the cabin, further reducing the number of passengers. Another FC-applicable liquid fuel is ammonia (NH_3), for which the recently growing prominence arises because of ammonia's relatively high chemical storage density. Taking NH_3 as a method to store H_2, the required 60 kg of H_2 involves about 340 kg of NH_3. The direct usage of NH_3 is currently efficient only with high-temperature solid-oxide fuel cells (SOFC), but several practical challenges remain, as recently highlighted by Jeerh *et al.* [57]. Overall, for PEM-based FCPS, LH_2 remains one of the most attractive candidates among the considered carbon-neutral fuels.

To propose the size of LH2 tanks, we first consider the space required to fit the selected four FC-stacks. The largest dimension of the Ballard FCgen®-HPS [53] is 0.555 m, leaving the available cabin height ≤0.815 m). Taking the LH_2 storage to be achieved with two identical cylindrical tanks (Figs. 3 and 4), each tank, when arranged horizontally, could be ~1.8 m long with ~0.74 m outer diameter. Figure 8 presents the proposed FCPS for Cessna 208 Caravan and the location of the LH_2 tanks, with a list of new and exchanged components, their volume and weights. Note that the weight calculations in Fig. 8 do not consider supplementary components such as supporting structures to secure the equipment rigidly in place, piping, high voltage cables, *etc*., all of which are relatively small in size but would add significant weight contributions. However, the presented calculations show weight savings >200 kg, which should serve as an allowance for the supplementary components. Hence, the proposed retrofit is expected to be of similar weight or lighter than the original Cessna 208 Caravan, especially with the expected progress in LH2 storage technologies.

Compared to the available power systems in aviation, FCPS has a low power density, although the potential for improvement is significant [1]. In the proposed retrofit for Cessna 208 Caravan, the main drawback arising from the low power density of FCPS has been discussed, namely that the total number of passengers allowable in the aircraft needs to be reduced from 14 to 8 to allow for the weight and volume of the FC stacks and LH2 storage tanks. This drawback can be reframed for the overall mission, namely that we would need two retrofitted aircraft to transport the same amount of people and fulfil the same mission as the original Cessna 14-passenger plane.

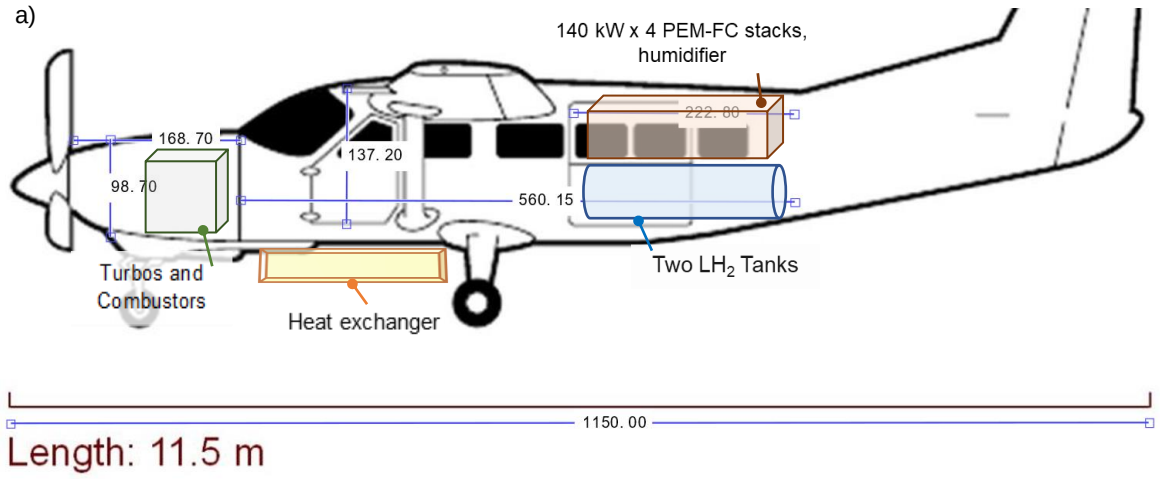

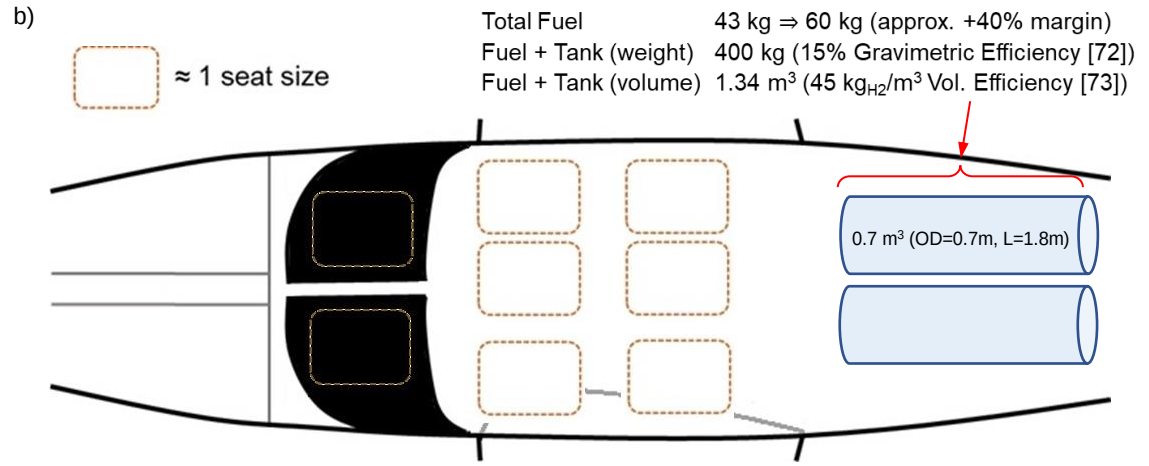

Original Items in Cessna 208 Caravan	Weight (kg)	[Ref.]	New components to replace	Weight (kg)	[Ref.]
Usable Jet Fuel	1009	[14]	Total H_2 fuel for short haul flight	60	Calculated
Tank	*Stored in Wings*		2 × LH_2 Tank	340	Calculated
PT6A-114A Engine	163	[75]	Magni 500	135	[76]
Three passengers	264	[71]	Total FCPS	615	Calculated
Total	(1436)		Total	1150	

PEM-FC Stacks **with cooling subsystem*	≈ 540 kg	[21, 24]
Turbochargers	≈ 28 kg	[77]
Heat Exchangers	≈ 26 kg	[44]
Humidifiers	≈ 13 kg	[78]
Combustor	≈ 8 kg	[79, 80]

Figure 8. a) FCPS retrofit proposal in Cessna 208 Caravan showing approximate locations and volume taken by the systems, b) Cessna 208 Caravan cabin compartment showing possible tank locations and estimated weight of replacing components. Cessna 208 Caravan diagram taken and edited from Lacoste [81].

5. Conclusions

In conclusion, a turbocharged multi-stack FCPS for aircraft applications was designed and modelled in MATLAB. The system was developed as a potential retrofit for an electric version of the Cessna 208 Caravan, equipped with a 560 kW_{el} electric propulsion system. The system contained four Ballard PEM-FC stacks, each rated at 140 kW_{el}, with two Garrett G25-550 turbochargers. Steady-state responses of the FCPS were simulated across a representative flight mission: 1.5 h long, covering more than 350 km as constructed using the aircraft flight manual. At least 41 kg of H_2 was

required to complete the mission using four stacks with equally shared power mode. Up to 10% more fuel would be needed if one stack were inactive from the start of the cruise phase, either due to a planned deactivation (daisy-chained power-sharing) or a stack failure encountered and isolated. Failure analysis on the overall FCPS demonstrated that the system reaches an overall failure rate as low as for a jet engine used in commercial aircraft. Results from the steady-state response study were used in sizing appropriate LH_2 storage tanks and other components of the potential FCPS for retrofitting Cessna 208 Caravan. A fully H_2-powered commercial aircraft, carrying up to 8 passengers and performing flight missions constructed in this paper was found feasible and warrants further study.

Acknowledgements

The authors thank Mr Henry Clarke from Stratospheric Platforms Ltd and Dr Marcus Clover for their advice and discussions.

Nomenclature

A	Area (cm^2 or m^2)
C	Ratio of capacity rate
C_w	Water concentration (mol cm^{-3})
c_p	Specific heat capacity (kJ kg^{-1} K^{-1})
D	Diffusion coefficient (cm^2 s^{-1})
E	Cell potential or voltage (V)
F	Faraday constant (C mol^{-1})
ΔG	Gibbs free energy (kJ mol^{-1})
LHV	Low heating value (kJ kg^{-1})
$\Delta \hat{H}$	Specific enthalpy (kJ kg^{-1})
HHV	High heating value (kJ kg^{-1})
i	Current density (A cm^{-2})
$M_{equiv,dry}$	Dry equivalent weight (kg mol^{-1})
$\dot{m}$	Mass flowrate (kg s^{-1})
NTU	Number of transfer unit
N_i	Number of *"i"*
P	Pressure (bar)
P_R	Pressure ratio
p	Partial pressure (bar)
Pow	Power (kW or shp)
R	Universal gas constant (J mol^{-1} K^{-1})
RH	Relative humidity
Q	Heat transferred (W)
T	Temperature (K or ℃)
U	Overall heat transfer coefficient (W m^{-2} K^{-1})
$\dot{W}$	Work required/obtained (kJ s^{-1})
ϵ	Effectiveness factor
η	Efficiency (%)
γ_{rf}	Electrode roughness factor
γ_i	Heat capacity ratio
λ	Membranes water activity
σ	Membrane conductivity (℧ cm^{-1})
ρ	Density (kg cm^{-3})

Subscripts

act	Activation
C	Compressor
$conc$	Concentration
$comb$	Combustor
el	Electrical
exh	Exhaust
FC	Fuel cell
H_2	Hydrogen
H_2O	Water
HT	Heat transfer
in	Inlet
L	Limiting
$mech$	Mechanical
mem	Membrane
O_2	Oxygen
$obt.$	Obtained
oc	Open-circuit
out	Outlet

		ref	Reference
Greek Letters		$req.$	Required
		T	Turbine
α	Charge transfer coefficient	$trans$	Transferred
δ	Membrane thickness (cm)	WT	Water transfer

References

[1] T. Kadyk, C. Winnefeld, R. Hanke-Rauschenbach, U. Krewer, Analysis and Design of Fuel Cell Systems for Aviation, Energies. 11 (2018) 375. https://doi.org/10.3390/en11020375.

[2] Department for Business, Energy & Industrial Strategy, £84 million boost for technology to power a green aviation revolution, GOV.UK. https://www.gov.uk/government/news/84-million-boost-for-technology-to-power-a-green-aviation-revolution (accessed December 21, 2021).

[3] R. K. Ahluwalia, C. F. Cetinbas, J.-K. Peng, X. Wang, and D. Papadias, Total Cost of Ownership (TCO) Analysis of Hydrogen Fuel Cells in Aviation - Preliminary Results, H2@Airports Workshop, (2020).

[4] J. Hoeflinger, P. Hofmann, Air mass flow and pressure optimisation of a PEM fuel cell range extender system, International Journal of Hydrogen Energy. 45 (2020) 29246–29258. https://doi.org/10.1016/j.ijhydene.2020.07.176.

[5] K. Murugesan, U. Subramaniam, Characterization and experimental validation of a semi-empirical fuel cell model for investigating the water dynamics on the electrical behavior of a 5 kW Ballard stack system using Nafion 117 polymer membrane, Journal of Renewable and Sustainable Energy. 12 (2020) 024301. https://doi.org/10.1063/1.5121609.

[6] Z. Abdin, C.J. Webb, E.MacA. Gray, PEM fuel cell model and simulation in Matlab–Simulink based on physical parameters, Energy. 116 (2016) 1131–1144. https://doi.org/10.1016/j.energy.2016.10.033.

[7] A. Kerviel, A. Pesyridis, A. Mohammed, D. Chalet, An Evaluation of Turbocharging and Supercharging Options for High-Efficiency Fuel Cell Electric Vehicles, Applied Sciences. 8 (2018) 2474. https://doi.org/10.3390/app8122474.

[8] Q. Xun, Y. Liu, X. Huang, E.A. Grunditz, J. Zhao, N. Zhao, Drive Cycle Energy Efficiency of Fuel Cell/Supercapacitor Passive Hybrid Vehicle System, IEEE Transactions on Industry Applications. 57 (2021) 894–903. https://doi.org/10.1109/TIA.2020.3035551.

[9] D. Guida, M. Minutillo, Design methodology for a PEM fuel cell power system in a more electrical aircraft, Applied Energy. 192 (2017) 446–456. https://doi.org/10.1016/j.apenergy.2016.10.090.

[10] T. Kadyk, R. Schenkendorf, S. Hawner, B. Yildiz, U. Römer, Design of Fuel Cell Systems for Aviation: Representative Mission Profiles and Sensitivity Analyses, Frontiers in Energy Research. 7 (2019) 35. https://doi.org/10.3389/fenrg.2019.00035.

[11] S. Campanari, G. Manzolini, A. Beretti, U. Wollrab, Performance Assessment of Turbocharged Pem Fuel Cell Systems for Civil Aircraft Onboard Power Production, Journal of Engineering for Gas Turbines and Power. 130 (2008). https://doi.org/10.1115/1.2772636.

[12] S. Atreya, M. Mata, R. Jones, L. Kohout, Power System Comparisons for a High Altitude Long Endurance (HALE) Remotely Operated Aircraft (ROA), in: AIAA 5th ATIO And16th Lighter-Than-Air Sys Tech. and Balloon Systems Conferences, American Institute of Aeronautics and Astronautics, 2012. https://doi.org/10.2514/6.2005-7401.

[13] Y.S. Kang, B.J. Lim, B.J. Cha, Multi-stage turbocharger system analysis method for high altitude UAV engine, J Mech Sci Technol. 31 (2017) 2803–2811. https://doi.org/10.1007/s12206-017-0523-4.

[14] Textron Aviation Inc., Versatility redefined: The Caravan fleet, BROCH-TBP-208A-071, 2016.

[15] P.A. Badell, Quick Look: Cessna 208 Caravan, (2016). https://www.aopa.org/news-and-media/all-news/2016/december/pilot/turbine-pilot-quick-look-cessna-208 (accessed December 22, 2021).

[16] G. A. McCoy and J. G. Douglass, Premium Efficiency Motor Selection and Application Guide – A Handbook for Industry, Washington State University Energy Program, 2014, DOE/BP-34623-2.

[17] J. Hemmerdinger, All-electric Grand Caravan makes maiden flight, Flight Global. (2020). https://www.flightglobal.com/airframers/all-electric-grand-caravan-makes-maiden-flight/138600.article (accessed December 22, 2021).

[18] A. Ahmadiparidari, L.A. Curtiss, A. Salehi-Khojin, Long Life Fully Reversible Lithium-CO_2 Battery, Meet. Abstr. MA2019-02 (2019) 18. https://doi.org/10.1149/MA2019-02/1/18.

[19] Temporaty revision 208PHTR03 for Cessna Model 208 Series Pilot’s operating handbook and FAA approved airplane flight manuals, 2004.

https://usermanual.wiki/Document/Cessna208C208675HP1998POHCessnaCaravanupdatedto2004.2437920911/view (accessed December 22, 2021).

[20] M. Prussi, L. Lonza, Passenger Aviation and High Speed Rail: A Comparison of Emissions Profiles on Selected European Routes, Journal of Advanced Transportation. 2018 (2018) e6205714. https://doi.org/10.1155/2018/6205714.

[21] Ballard Power Systems Inc., FCveloCity®-HD, SPC5104967-0B, Product Data Sheet, 2018.

[22] Ballard Power Systems Inc., FCveloCity®-MD, SPC5105678-0A, Product Data Sheet, 2018.

[23] J. Han, J. Park, S. Yu, Control strategy of cooling system for the optimization of parasitic power of automotive fuel cell system, International Journal of Hydrogen Energy. 40 (2015) 13549–13557. https://doi.org/10.1016/j.ijhydene.2015.08.067.

[24] N. Konno, S. Mizuno, H. Nakaji, Y. Ishikawa, Development of Compact and High-Performance Fuel Cell Stack, SAE Int. J. Alt. Power. 4 (2015) 123–129. https://doi.org/10.4271/2015-01-1175.

[25] [1]Z. Liu, J. Chen, S. Chen, L. Huang, Z. Shao, Modeling and Control of Cathode Air Humidity for PEM Fuel Cell Systems, IFAC-PapersOnLine. 50 (2017) 4751–4756. https://doi.org/10.1016/j.ifacol.2017.08.943.

[26] L. Khotseng, Fuel Cell Thermodynamics, in: P. Vizureanu (Ed.), Thermodynamics and Energy Engineering, IntechOpen, 2020, pp. 1-17. https://doi.org/10.5772/intechopen.90141.

[27] A.L. Lazar, S.C. Konradt, H. Rottengruber, Open-Source Dynamic Matlab/Simulink 1D Proton Exchange Membrane Fuel Cell Model, Energies. 12 (2019) 3478. https://doi.org/10.3390/en12183478.

[28] C. Spiegel, Designing and Building Fuel Cells, McGraw-Hill Professional, 2007, p. 251. https://doi.org/10.1036/9780071510639.

[29] J. Thangavelautham, Degradation in PEM Fuel Cells and Mitigation Strategies Using System Design and Control, in: T. Taner (Ed.), Proton Exchange Membrane Fuel Cell, InTech, 2018, pp. 63-95. https://doi.org/10.5772/intechopen.72208.

[30] T. Thampan, S. Malhotra, J. Zhang, R. Datta, PEM fuel cell as a membrane reactor, Catalysis Today. 67 (2001) 15–32. https://doi.org/10.1016/S0920-5861(01)00278-4.

[31] J. Durst, C. Simon, F. Hasché, H.A. Gasteiger, Hydrogen Oxidation and Evolution Reaction Kinetics on Carbon Supported Pt, Ir, Rh, and Pd Electrocatalysts in Acidic Media, J. Electrochem. Soc. 162 (2014) F190. https://doi.org/10.1149/2.0981501jes.

[32] A.B. Anderson, J. Roques, S. Mukerjee, V.S. Murthi, N.M. Markovic, V. Stamenkovic, Activation Energies for Oxygen Reduction on Platinum Alloys: Theory and Experiment, J. Phys. Chem. B. 109 (2005) 1198–1203. https://doi.org/10.1021/jp047468z.

[33] J. Zhang, H. Zhang, J. Wu, J. Zhang, Chapter 10 - High-Temperature PEM Fuel Cells, in: J. Zhang, H. Zhang, J. Wu, J. Zhang (Eds.), Pem Fuel Cell Testing and Diagnosis, Elsevier, Amsterdam, 2013: pp. 243–282. https://doi.org/10.1016/B978-0-444-53688-4.00010-3.

[34] D.D. Papadias, R.K. Ahluwalia, N. Kariuki, D. Myers, K.L. More, D.A. Cullen, B.T. Sneed, K.C. Neyerlin, R. Mukundan, R.L. Borup, Durability of Pt-Co Alloy Polymer Electrolyte Fuel Cell Cathode Catalysts under Accelerated Stress Tests, J. Electrochem. Soc. 165 (2018) F3166. https://doi.org/10.1149/2.0171806jes.

[35] "NafionTM N115, N117, N1110, Ion Exchange Materials, Extrusion Cast Membranes," Product Bulletin P-12, C-10604 (2/16), The Chemours Company FC, Delaware, US, 2016.

[36] J.M. Correa, F.A. Farret, L.N. Canha, M.G. Simoes, An electrochemical-based fuel-cell model suitable for electrical engineering automation approach, IEEE Transactions on Industrial Electronics. 51 (2004) 1103–1112. https://doi.org/10.1109/TIE.2004.834972.

[37] Ballard Power Systems Inc., Fuel cell catalyst materials. Non-precious metal catalyst, Technical note, 2017.

[38] M. Oszcipok, M. Zedda, J. Hesselmann, M. Huppmann, M. Wodrich, M. Junghardt, C. Hebling, Portable proton exchange membrane fuel-cell systems for outdoor applications, Journal of Power Sources. 157 (2006) 666–673. https://doi.org/10.1016/j.jpowsour.2006.01.005.

[39] V. Liso, M.P. Nielsen, S.K. Kær, H.H. Mortensen, Thermal modeling and temperature control of a PEM fuel cell system for forklift applications, International Journal of Hydrogen Energy. 39 (2014) 8410–8420. https://doi.org/10.1016/j.ijhydene.2014.03.175.

[40] J. Larminie, A. Dicks, Appendix 2: Useful Fuel Cell Equations, in: Fuel Cell Systems Explained, John Wiley & Sons, Ltd, 2003: pp. 395–400. https://doi.org/10.1002/9781118878330.app2.

[41] A.R. Vijay Babu, P. Manoj Kumar, G. Srinivasa Rao, Parametric study of the proton exchange membrane fuel cell for investigation of enhanced performance used in fuel cell vehicles, Alexandria Engineering Journal. 57 (2018) 3953–3958. https://doi.org/10.1016/j.aej.2018.03.010.

[42] N. Hall, "Compressor Thermodynamics," Nasa.gov, May-2021. [Online]. Available: https://www.grc.nasa.gov/www/k-12/airplane/compth.html. [Accessed: 14-Dec-2021].

[43] N. Hall, “Power Turbine Thermodynamics,” Nasa.gov, May-2021. [Online]. Available: https://www.grc.nasa.gov/www/k-12/airplane/powtrbth.html. [Accessed: 14-Dec-2021].

[44] Garrett Turbo Performance Catalog, Garrett Motion Inc, California, US, 2019.

[45] P. Linstrom, NIST Chemistry WebBook, NIST Standard Reference Database 69, (1997). https://doi.org/10.18434/T4D303..

[46] J. Holman, Heat Transfer, 10th edition, McGraw-Hill Education, Boston, 2009, pp. 540–554.

[47] Overall Heat Transfer Coefficient Table Charts and Equation, Engineers Edge (2021). https://www.engineersedge.com/thermodynamics/overall_heat_transfer-table.htm (accessed December 22, 2021).

[48] S.-K. Park, S.-Y. Choe, T.-W. Lim, J.-S. Kim, D.-H. Seo, J.H. Choi, Analysis of a shell-and-tube type gas-to-gas membrane humidifier for an automotive polymer electrolyte membrane fuel cell power system, Int.J Automot. Technol. 14 (2013) 449–457. https://doi.org/10.1007/s12239-013-0049-4.

[49] Perma Pure LLC, FC Series Humidifiers| Consistent Humidification for High-Flow Applications, FC-Series-Flyer-1810, 2018.

[50] O. N. Favorsky, A-to-Z Guide to Thermodynamics, Heat and Mass Transfer, and Fluids Engineering: AtoZ, Begellhouse, 2006.

[51] P.P. Panda, E.S. Hecht, Ignition and flame characteristics of cryogenic hydrogen releases, International Journal of Hydrogen Energy. 42 (2017) 775–785. https://doi.org/10.1016/j.ijhydene.2016.08.051.

[52] J.C. Amphlett, R.F. Mann, B.A. Peppley, P.R. Roberge, A. Rodrigues, A practical PEM fuel cell model for simulating vehicle power sources, in: Proceedings of the Tenth Annual Battery Conference on Applications and Advances, 1995: pp. 221–226. https://doi.org/10.1109/BCAA.1995.398535.

[53] Ballard Power Systems Inc., FCgen®-HPS, SPC5109615-0A, Product Data Sheet, 2020.

[54] J. Cardozo, N. Marx, L. Boulon, D. Hissel, Comparison of Multi-Stack Fuel Cell System Architectures for Residential Power Generation Applications Including Electrical Vehicle Charging, in: 2015 IEEE Vehicle Power and Propulsion Conference (VPPC), 2015: pp. 1–6. https://doi.org/10.1109/VPPC.2015.7352912.

[55] N. Marx, L. Boulon, F. Gustin, D. Hissel, K. Agbossou, A review of multi-stack and modular fuel cell systems: Interests, application areas and on-going research activities, International Journal of Hydrogen Energy. 39 (2014) 12101–12111. https://doi.org/10.1016/j.ijhydene.2014.05.187.

[56] J. Yoon and R. Betancourt, Battery cell bypass switches – A case study in test like you fly merits, Proc. 18. European Space Mechanisms and Tribology Symposium 2019, Munich, 2019.

[57] G. Jeerh, M. Zhang, S. Tao, Recent progress in ammonia fuel cells and their potential applications, J. Mater. Chem. A. 9 (2021) 727–752. https://doi.org/10.1039/D0TA08810B..

[58] Engineering ToolBox, U.S. Standard Atmosphere vs. Altitude, (2003), https://www.engineeringtoolbox.com/standard-atmosphere-d_604.html (accessed December 22, 2021).

[59] M. Whiteley, A. Fly, J. Leigh, S. Dunnett, L. Jackson, Advanced reliability analysis of Polymer Electrolyte Membrane Fuel Cells using Petri-Net analysis and fuel cell modelling techniques, International Journal of Hydrogen Energy. 40 (2015) 11550–11558. https://doi.org/10.1016/j.ijhydene.2015.01.154.

[60] S. Collong, R. Kouta, Fault tree analysis of proton exchange membrane fuel cell system safety, International Journal of Hydrogen Energy. 40 (2015) 8248–8260. https://doi.org/10.1016/j.ijhydene.2015.04.101.

[61] T. LeCompte, Deadstick Landings, Air & Space/Smithsonian, (2010), https://www.geaviation.com/press-release/ge90-engine-family/record-year-worlds-largest-most-powerful-jet-engine. (accessed December 14, 2021).

[62] Record Year For The World's Largest, Most Powerful Jet Engine, GE Aviation, (2012). https://www.geaviation.com/press-release/ge90-engine-family/record-year-worlds-largest-most-powerful-jet-engine (accessed December 22, 2021).

[63] L. Piancastelli, Powerplant Reliability Issues and Wear Monitoring in Aircraft Piston Engines. Part II: Engine Diagnostic, Drones. 2 (2018) 10. https://doi.org/10.3390/drones2010010.

[64] S.J.C. Cleghorn, D.K. Mayfield, D.A. Moore, J.C. Moore, G. Rusch, T.W. Sherman, N.T. Sisofo, U. Beuscher, A polymer electrolyte fuel cell life test: 3 years of continuous operation, Journal of Power Sources. 158 (2006) 446–454. https://doi.org/10.1016/j.jpowsour.2005.09.062.

[65] UK Health and Safety Executive, Failure Rate and Event Data for use within Risk Assessments (06/11/17), PCAG chp_6K Version 14, 2017.

[66] U.S. Department of Defense, Military handbook: Reliability Prediction of Electronic Equipment MIL-HDBK-217F, Notice 2,1995.

[67] L.C. Cadwallader, Selected component failure rate values from fusion safety assessment tasks, Idaho National Lab. (INL), Idaho Falls, ID (United States), 1998. https://doi.org/10.2172/752571.

[68] D.G.S. Prayoga, D. Priyanta, N. Siswantoro, Comparative Analysis of Probability of Failure Determination Using Weibull Distribution and Generic Failure Frequencies on Heat Exchanger Tube Bundles Based on API 581, International Journal of Marine Engineering Innovation and Research. 2 (2018). https://doi.org/10.12962/j25481479.v2i3.3576.

[69] F. Gaspari, L. Trainelli, A. Rolando, and I. Perkon, D1.1: Concept of Modular Architecture for Hybrid Electric Propulsion of Aircraft, Mahepa Project report, Ref. Ares(2017)5981497, 2017.

[70] H. Paul Barringer, Reliability of critical turbo/compressor equipment, Fifth International Conference on Process Plant Reliability, 1996.

[71] Z. Berdowsk, F.N. van den Broek-Serlé, J.T. Jetten, Y. Kawabata, J.T. Schoemaker, R. Versteegh, Survey on standard weights of passengers and baggage, EASA Report R20090095, 2009.

[72] Fuel Cells and Hydrogen 2 Joint Undertaking, Hydrogen-powered aviation: a fact based study of hydrogen technology, economics, and climate impact by 2050, Publications Office, LU, 2020. https://data.europa.eu/doi/10.2843/471510.

[73] E. Rivard, M. Trudeau, K. Zaghib, Hydrogen Storage for Mobility: A Review, Materials. 12 (2019) 1973. https://doi.org/10.3390/ma12121973.

[74] Ó. González-Espasandín, T.J. Leo, M.A. Raso, E. Navarro, Direct methanol fuel cell (DMFC) and H_2 proton exchange membrane fuel (PEMFC/H2) cell performance under atmospheric flight conditions of Unmanned Aerial Vehicles, Renewable Energy. 130 (2019) 762–773. https://doi.org/10.1016/j.renene.2018.06.105.

[75] European Aviation Safety Agency, EASA Type – Certificate Data Sheet, PT6A-100 series engines, IM.E. 094 (2014) 2.

[76] J. Richardson, 750 Horsepower Electric Aviation Engine Tested By MagniX, CleanTechnica. (2019). https://cleantechnica.com/2019/10/24/750-horsepower-electric-aviation-engine-tested-by-magnix/ (accessed December 22, 2021).

[77] Garrett G25-550 Turbocharger, Turbomotiv. (2021). https://www.turbomotiv.com/product/garrett-g25-550-turbocharger/ (accessed December 22, 2021).

[78] E.J. Carlson, P. Kopf, J. Sinha, S. Sriramulu, Y. Yang, Cost Analysis of PEM Fuel Cell Systems for Transportation, 2005. https://doi.org/10.2172/862302.

[79] Changsha Guanghua Aviation Technology Co., Ltd, GT25 2-Stroke RC Gasoline Engines. https://www.nghengine.com/product/7.html?productCateId=9 (accessed December 22, 2021).

[80] Changsha Guanghua Aviation Technology Co., Ltd, GT35 2-Stroke RC Gasoline Engines. https://www.nghengine.com/product/15.html (accessed December 22, 2021).

[81] M. Lacoste, Cessna 208 Caravan three views. https://commons.wikimedia.org/wiki/File:Caravan_three_views.png (accessed December 22, 2021).